Steric Impediment of Ion Migration Contributes to Improved Operational Stability of Perovskite Solar Cells

Shaun Tan, Ilhan Yavuz, Nicholas De Marco, Tianyi Huang, Sung-Joon Lee, Christopher S. Choi, Minhuan Wang, Selbi Nuryyeva, Rui Wang, Yepin Zhao, Hao-Cheng Wang, Tae-Hee Han, Bruce Dunn, Yu Huang, Jin-Wook Lee and Yang Yang**

S. Tan, N. D. Marco, T. Huang, S.-J. Lee, C. S. Choi, M. Wang, S. Nuryyeva, R. Wang, Y. Zhao, H.-C. Wang, Prof. T.-H. Han, Prof. B. Dunn, Prof. Y. Huang, Prof. J.-W. Lee and Prof. Y. Yang

Department of Materials Science and Engineering and California NanoSystems Institute, University of California Los Angeles, Los Angeles, CA 90095, USA
E-mail: J.-W. Lee: jw.lee@skku.edu, Y.Yang: yangy@ucla.edu

Prof. I. Yavuz
Department of Physics, Marmara University, 34722, Ziverbey, Istanbul, Turkey

Prof. T.-H. Han

Division of Materials Science and Engineering, Hanyang University, Seoul 04763, Republic of Korea

Prof. J.-W. Lee

SKKU Advanced Institute of Nanotechnology (SAINT) and Department of Nanoengineering, Sungkyunkwan University, Suwon 16419, Republic of Korea

Keywords: ion migration, stability, steric engineering, perovskite solar cells, acetamidinium

The operational instability of perovskite solar cells (PSCs) is known to mainly originate from the migration of ionic species (or charged defects) under a potential gradient. Compositional engineering of the 'A' site cation of the ABX_3 perovskite structure has been shown to be an effective route to improve the stability of PSCs. Here, we investigate the effect of size-mismatch-induced lattice distortions on the ion migration energetics and operational stability of PSCs. We observed that the size mismatch of the mixed 'A' site composition films and devices led to a steric effect to impede the migration pathways of ions to increase the activation energy of ion migration, which we demonstrate through multiple theoretical and experimental evidence. Consequently, the mixed composition devices exhibited significantly improved thermal stability under continuous heating at 85 °C and operational stability under continuous 1-sun illumination, with an extrapolated lifetime of 2,011 h, compared to the 222 h of the reference device.

This is the author manuscript accepted for publication and has undergone full peer review but has not been through the copyediting, typesetting, pagination and proofreading process, which may lead to differences between this version and the Version of Record. Please cite this article as doi: 10.1002/adma.201906995.

Introduction

In just a decade of unprecedented progress,[1–8] the record power conversion efficiencies (PCEs) of lead halide perovskite solar cells (PSCs) have propelled from an initial 3.8% to over 23%. Despite the impressive evolution, the notorious instability of PSCs remains a major challenge standing in the way of commercialization. Accelerated degradation upon exposure to external environmental factors including moisture, heat, oxygen, or ultraviolet illumination have been well documented.[9–13] More importantly, due to the ionic nature of perovskite materials, and the low formation[14] and migration activation energies[15,16] of the ionic species, a large number of the ions are mobile in the presence of a potential gradient, and this has been shown to have significant negative repercussions on the long-term operational stability of PSCs since mobile ions can migrate towards and into the adjacent contact layers to rupture the perovskite lattice and degrade the charge extracting/transporting functionality of the contacting layers.[15,17–19]

Various strategies have been reported to enhance the stability of PSCs. Particularly, compositional engineering involves substituting or replacing the 'A' site cation or 'X' site anion in the $APbX_3$ (X is one of or a mixed of I^-, Cl^- or Br^-) perovskite lattice.[20–22] Compositional engineering of the 'X' site anion by substitution of I^- to create mixed halide compositions have been reported to enhance the chemical and environmental stability of PSCs,[23–25] For instance, substitution of I^- with the more electronegative Br^- increases the bonding strength with the perovskite lattice to enhance its stability,[26] but halide substitution increases the optical bandgap of the perovskite to sacrifice its photocurrent. Furthermore, mixed halide PSCs suffer from poor operational stability due to phase segregation of the halide anions under illumination.[24,27]

On the other hand, modulation of the 'A' site cation has proven to be effective to enhance both the performance and stability without significantly altering the optoelectronic properties of the original perovskite composition. Compositional engineering of the 'A' site cation to incorporate formamidinium ($(NH_2)_2CH^+$, FA), guanidinium ($CH_6N_3^+$, GA), Cs and/or Rb have delivered high efficiencies as well as significantly improved stability over the commonly used pure methylammonium ($CH_3NH_3^+$, MA) composition.[28–30] However, the improved operational stability of mixed 'A' site compositions has yet been fully elucidated. For example, the substitution of MA for GA was previously shown to enhance the stability of the mixed MA/GA devices, attributed only to the enhanced hydrogen bonding strength of GA with the lattice due to the two additional amine groups of GA.[28] However, the improved stability was not fully elucidated in terms of changes in the local lattice structure which might be more closely related to ion migration. Particularly, the possible change in the ion migration pathway and energetics as a result of localized lattice distortions caused by the much larger size of GA relative to MA was not investigated. It was recently suggested that 'A' cation compositional engineering can introduce localized distortions to the perovskite lattice structure in an attempt to control the energetics of ion migration.[31] However, it was challenging to decouple the steric impediment effect on ion migration due to the localized lattice distortions from the contribution of hydrogen bonding,[31] which was not further correlated with device stability. Understanding the relationship between 'A' cation size, hydrogen bonding, ion migration, and device operational stability would provide essential knowledge towards designing more operationally stable perovskite compositions.

In this work, we investigate the effect of 'A' cation size mismatch on the ion migration energetics and operational stability of PSCs. Partially substituting small MA with a larger 'A' site cation is expected to locally distort the perovskite lattice in order to fit the larger cation. The effect of this on the perovskite ion migration energetics has not been independently studied before due to the difficulty in separating the contributions of 'A' cation hydrogen bonding vs size. We systematically decoupled both effects by strategically choosing a suitable 'A' cation (acetamidinium (Ace), $CH_3C(NH_2)^{2+}$). Our work showcases a new strategy to utilize 'A' cation size mismatch to improve the operational stability of perovskites solar cells.

Decoupling size versus hydrogen bonding effect

We first had to find a suitable ‘A’ cation that will allow us to study only the ‘A’ cation size effect and decouple the hydrogen bonding effect. From our initial screening, we thought that Ace **(Figure 1a)** might be suitable due to its ionic radius (277 pm)[32] being considerably larger than MA (Figure 1b, 217 pm),[33] and being similar in size with GA (Figure 1c, 278 pm).[28] On the other hand, we speculated that Ace would probably have a weaker hydrogen bond interaction with the perovskite lattice due to its one less amine group compared to GA. The large size of Ace (or GA) means that the calculated tolerance factor (*t*) value of $AcePbI_3$ of 1.03 is above the theoretical range by which the cubic perovskite structure can form.[33] We confirmed that pure $AcePbI_3$ does not form the perovskite phase using X-ray diffraction (XRD) on the as-prepared $AcePbI_3$ film (Figure S1). Conversely, $MAPbI_3$ (t=0.91) is known to crystallize in the less symmetrical tetragonal I4/*mcm* phase at room temperature[34] instead of the more ideal cubic phase since MA is too small. Partial substitution of MA with Ace to create a binary mixed cation $Ace_xMA_{1-x}PbI_3$ composition should compensate the two size extremes to tune the tolerance factor of $MAPbI_3$ upwards to within the desired cubic phase range. If so, the unit cell would have to expand to accommodate space to fit the larger Ace.

To empirically justify the choice of Ace for our study, we compared the hydrogen bonding interaction of MA, Ace and GA with the perovskite lattice using density functional theory (DFT) simulations. We modelled the ground state unit cell with the different ‘A’ cations and included the hydrogen bonds within a standard H-I bond length (2.5 – 3.5 Å)[35] and N-H-I bond angle > 110° (**Table 1**) in accordance with the recommended definition of a hydrogen bond by IUPAC[36] to arrive at the effective number of hydrogen bonds of Ace (3), MA (3), and GA (7), as shown in Figure 1d-f. The results show that MA and Ace have the same number of effective hydrogen bonds, and is less than half that of GA. This is supported by the thermogravimetric (TGA) results (Figure S2). As previously reported, the steps at approximately 100 °C, 300 °C and 450 °C are due to the sublimation of DMSO, MAI and PbI_2, respectively.[37] We observed from the first derivative weight loss curves that the sublimination peaks around 350 °C is comparable for pure $MAPbI_3$ and the Ace-containing perovskite, indicating that the hydrogen bond strengths of MA and Ace with the perovskite are comparable. Therefore, we assumed that a difference in ion migration energetics between Ace and MA, if any, should be due primarily to the size-mismatch-induced lattice distortions.

Computational study of ion migration energetics

We hypothesized that the localized lattice distortions caused by the size mismatch between Ace and MA might constitute a steric impediment effect to disrupt the pathways by which ions migrate. To study this effect theoretically, we performed further DFT simulations to model the ion migration pathway in the unit cell (**Figure 2a-d**) and to calculate the activation energy for the migration (Figure 2e). We chose to focus on the iodide ion transport since it was reported to have the lowest activation energy[15,16] and is thus the most prone to migrate/diffuse. Figure 2a and c (side view) and Figure 2b and d (top view) are overlays of 18 different structures corresponding to the 18 steps in Figure 2e used to define the initial and final positions of the iodide ion during the migration. The calculated activation energy is 0.40 eV for $MAPbI_3$, consistent with previously reported values.[16,31,38] For the mixed $Ace_{0.25}MA_{0.75}PbI_3$ system, the activation energy is increased to 0.63 eV. The increased barrier height is probably due to steric impediment caused by the size-mismatch-induced lattice distortions, which can clearly be seen in the simulated migration pathway for the $Ace_{0.25}MA_{0.75}PbI_3$ system in Figure 2d, where the iodide ion should first curves inwards, then outwards, from the unit cell, as compared to the simple linear path of $MAPbI_3$ during the migration (Figure 2b). Importantly, we observe through the transition state structures in Figure 2e that the H-I bond length between the nearest neighboring hydrogen and the migrating iodide ion (highlighted in green) is significantly greater for $Ace_{0.25}MA_{0.75}PbI_3$ (3.10 Å) compared to $MAPbI_3$ (2.64 Å), indicating a much weaker H-I bond interaction between Ace and the mobile iodide. This, in addition to the overall weaker hydrogen bonding between Ace and the perovskite lattice discussed above, indicates that the steric impediment effect is mainly responsible for the increased activation energy barrier.

Since Ace (277 pm) and GA (278 pm) have almost identical ionic radii, we expect the lattice volume expansion by replacing MA with either to be similar. We calculated the unit cell volume from our simulated models of $Ace_{0.25}MA_{0.75}PbI_3$ and $GA_{0.25}MA_{0.75}PbI_3$ (supplemental note 1) and found that both are identical at 253 $Å^3$ (for the Ace or GA containing unit cell), whereas pure $MAPbI_3$ has a unit cell volume of 248 $Å^3$. We then additionally simulated the energy barrier for $GA_{0.25}MA_{0.75}PbI_3$ (Figure S3) and expectedly found that the ion migration activation energy is the highest at 0.73 eV since for $GA_{0.25}MA_{0.75}PbI_3$, both steric impediment and hydrogen bonding contributes to impede ion migration. Therefore, comparing $MAPbI_3$ and $Ace_{0.25}MA_{0.75}PbI_3$ allows us to only study the effect of steric impediment (since Ace is larger than MA but has same number of effective hydrogen bonds). When comparing $MAPbI_3$ and $GA_{0.25}MA_{0.75}PbI_3$, both effects (since GA is larger and has higher number of effective hydrogen bonds than MA) influence the ion migration energetics, so it is not possible to distinguish one effect from the other.

Size-mismatch-induced lattice expansion and optical properties of the films

After justifying that the steric impediment effect can only be studied by comparing $MAPbI_3$ and $Ace_xMA_{1-x}PbI_3$, we subsequently fabricated $Ace_xMA_{1-x}PbI_3$ films to investigate the lattice distortions caused by the size mismatch between Ace and MA. XRD measurements were performed on mixed composition $Ace_xMA_{1-x}PbI_3$ films, where x was varied from 0 ($MAPbI_3$) to 1.00 ($AcePbI_3$). As shown in **Figure 3a**, the tetragonal perovskite phase is retained without formation of any secondary phases up to x = 0.2. Figure S4 displays the individual diffractograms in logarithmic scale for additional clarity. The (110) perovskite diffraction peak intensity was generally maintained except for x = 0.10, although the apparent grain size observed from the top surface scanning electron microscopy (SEM) images (Figure S5 and S6) of the films seemed to decrease, indicating that the bulk crystal quality might be improved with incorporation of Ace. We reasoned that the reduced apparent grain size is possibly due to the incorporated Ace acting as heterogenous nucleation sites to increase the nucleation rate, whereas the more ideal tolerance factor with incremental substitution of Ace is probably responsible for the improved bulk crystal quality as observed previously by the enhanced crystallinity of $FA_{1-x}Cs_xPbI_3$ and $FA_{1-x}MA_xPbI_3$ films relative to the pure $FAPbI_3$ film.[39–42] At x = 0.2, additional diffraction peaks at ~11.3° and ~25.3° began to emerge, which indicates that Ace can no longer incorporate into the perovskite lattice and thus formed the secondary $AcePbI_3$ phase. Additionally, X-ray photoelectron spectroscopy (XPS) measurements (Figure S7) on the $Ace_xMA_{1-x}PbI_3$ films further demonstrate the substitution of MA with Ace. The raw data was deconvoluted to reveal two constituent profiles attributed to the N 1s peaks originating from the NH_3^+ group in MA at ~402.3 eV and the NH_2^+ group in Ace at ~400.6 eV. The fitted profiles were used to calculate the Ace percentage in the films (Figure S7b), which closely match those of the nominal compositions in the precursor solutions.

High-resolution XRD measurements were carried out to investigate the lattice parameter changes, where the diffractograms were carefully calibrated with the constant PbI_2 peak at ~12.6° (Figure 3b). The results show that the (110) perovskite peak incrementally shifted towards lower 2θ angles with incorporation of Ace, indicating an expansion of the lattice due to the substitution of the smaller MA with the larger Ace. The *a* (or *b*) and *c* unit cell parameters for the films were extracted from the diffractograms as shown in Figure 3c, which shows that *a* (or *b*) increased with increasing incorporation of Ace from 8.867 Å for x = 0 to 8.913 Å for x = 0.2 (ca. 0.5% increment), whereas *c* increased marginally. We additionally measured the XRD diffractograms of $GA_xMA_{1-x}PbI_3$ (Figure S8) to compare the lattice volume expansions given by the ratio (unit cell volume of $Ace_xMA_{1-x}PbI_3$ or $GA_xMA_{1-x}PbI_3$)/(unit cell volume of $MAPbI_3$). The volume expansion is nearly identical (Figure S9) for $Ace_xMA_{1-x}PbI_3$ and $GA_xMA_{1-x}PbI_3$ due to the similarity in size between Ace and GA.

The absorption and normalized steady-state photoluminescence (PL) spectra of the $Ace_xMA_{1-x}PbI_3$ films are shown in Figure 3d. For x < 0.2, both the absorption profiles and the peak PL positions of the films were nearly identical with bare $MAPbI_3$ (x = 0), indicating that the films retained the optical properties of $MAPbI_3$ at relatively low levels of Ace incorporation. Further addition of Ace above x > 0.2 was seen to decrease the absorption of the films across all measured wavelengths, which can be attributed to the formation of the non-perovskite $AcePbI_3$ phase. Despite the substitution of MA with Ace, the absorption onsets were nearly unchanged (Figure S10), indicating that the bandgap of the mixed composition films remained roughly identical. The PL spectra redshifted and broadened asymmetrically, likely due to formation of the secondary phase that possibly introduced shallow defects at the band edges.

Device photovoltaic performance, charge carrier lifetimes and diode characteristics

To investigate the photovoltaic performance of the $Ace_xMA_{1-x}PbI_3$ perovskites, we fabricated planar n-i-p solar cell devices of structure ITO/SnO_2/perovskite/spiro-MeOTAD/Au. Based on tolerance factor considerations, pristine $MAPbI_3$ has a tetragonal crystal structure due to the small size of MA,[34] which implies that $MAPbI_3$ is intrinsically strained compressively. As previously reported, substitution of MA with a larger cation like FA or GA can compensate this intrinsic compressive strain and increase the tolerance factor towards 1 to improve the device photovoltaic performance.[28,39,43,44] Therefore, we speculated that the incorporation of Ace up to a certain limit should also improve the device performance. The photovoltaic parameters of the devices with different Ace substitution levels are summarized in **Table 2** and Figure S11. The average photovoltaic parameters (sample size, *n* = 25) of the reference $MAPbI_3$ devices (hereafter referred to as MA) are short-circuit current density (J_{SC}): 22.59 ± 0.14 mA cm^{-2}, open-circuit voltage (V_{OC}): 1.105 ± 0.007 V, fill factor (FF): 0.710 ± 0.012, and power conversion efficiency (PCE): 17.72 ± 0.34 %. Systematic variation of the Ace substitution level determined that $Ace_{0.03}MA_{0.97}PbI_3$ (henceforth denoted as

AceMA) exhibited the best device performance, with an average ($n = 43$) J_{SC} of 22.67 ± 0.15 mA cm^{-2}, V_{OC} of 1.134 ± 0.009 V, FF of 0.750 ± 0.013, to yield a PCE of 19.28 ± 0.44 % (8.8% improvement over the average PCE of 17.72 ± 0.34 % for the MA devices). The PCE enhancement was due to the increased V_{OC} and FF, whereas the J_{SC} remained nearly identical. The distribution of the photovoltaic parameters of the MA and AceMA devices are compared in box plots as shown in **Figure 4a** and Figure S12. We note that the devices were fabricated across multiple batches to demonstrate the reproducibility of the results.

The current density and voltage (*J*-*V*) curves of the champion devices are displayed in Figure 4b. Ultimately, the champion AceMA device attained a PCE of 20.30 % with a J_{SC} of 22.88 mA cm^{-2}, V_{OC} of 1.143 V, and FF of 0.776, while the champion MA device had a PCE of 18.49 % (J_{SC}: 22.80 mA cm^{-2}, V_{OC}: 1.108 V, FF: 0.732). The external quantum efficiency (EQE) spectra of the AceMA and MA devices are shown in Figure S13. The integrated J_{SC} calculated from the EQE spectra for the AceMA device was 22.02 mA cm^{-2}, within reasonable discrepancy (< 4%) from the measured J_{SC} from the *J*-*V* scans. However, the integrated J_{SC} for the MA device was 21.62 mA cm^{-2}, a comparatively large 5.5% discrepancy compared to the J_{SC} obtained from the *J*-*V* scans, which suggests an increased capacitive current effect due to more pronounced ion migration.[45] The stabilized PCEs were measured to be 19.5 % and 17.1 % for the champion AceMA and MA devices, respectively, as shown in inset Figure 4b and Figure S14. The smaller discrepancy between the stabilized PCE and the *J*-*V* scan obtained PCE for the AceMA device also implies suppressed hysteresis and ion migration, which is further evident in the scan direction dependent *J*-*V* curves of Figure S15.

To elucidate the origin of the improved photovoltaic performance of the mixed composition AceMA devices, we first measured the steady-state and time-resolved photoluminescence (PL) of the perovskite films deposited on glass substrates to study the charge recombination dynamics of the films (inset Figure 4c). The steady-state PL peak intensity increased by 43.7% from ~1.53 $\times 10^6$ for MA to ~2.20 $\times 10^6$ for AceMA, indicating an enhanced radiative recombination with substitution of 3 mol% MA for Ace. The time-resolved PL measurement showed that the improved radiative recombination is due to an enhanced PL lifetime, where the curves were fitted with a bi-exponential model (Figure 4c), with fitted parameters presented in **Table 3**. Two decay regimes are distinguishable from the fits, where the initial fast decay regime (A_1 and τ_1) is assigned to non-radiative carrier recombination induced by deep trap states such as structural disorders, whereas the subsequent slow decay regime (A_2 and τ_2) is ascribed to radiative recombination in the bulk perovskite.[46,47] For the AceMA film, we calculated that the fast decay carrier lifetime (τ_1) increased from 10.4 ns to 20.4 ns, and the proportion of fast decay (A_1) decreased from 83.6 % to 76 %, indicating reduced trap-mediated non-radiative recombination loss. τ_2 also increased from 180.7 ns for MA to 205.9 for AceMA. Resultantly, the average carrier lifetime was elongated from 38.3 ns to 64.9 ns for the MA and Ace films, respectively. We speculate that the enhanced steady-state PL and charge carrier lifetime for AceMA is a result of an improved bulk crystal quality due to the more ideal tolerance factor by replacing the too small MA with Ace.

The charge carrier lifetime within the complete device was also investigated with transient photovoltage (TPV) measurements at open-circuit condition, as shown in Figure 4d. Upon illumination with a pulsed light, electrons and holes are photogenerated to constitute the photovoltage, and subsequently recombine with elimination of the light source, which is observed as the decay in photovoltage. The rate with which the photovoltage decays is correlated with the charge carrier lifetime in the device. The decay time constants were extracted from the raw data using a mono-exponential decay function, with the fitted functions shown in Figure 4d as solid lines. The decay time constant was increased from 1.70 μs for the MA device to 2.28 μs for the AceMA device, indicating that the latter has much longer charge carrier lifetime in the device, consistent with the steady-state and time-resolved PL results.

Since the improved photovoltaic performance of the AceMA device is due to the increased V_{OC} and FF, we additionally measured the dark *J-V* response of the complete devices to extract the shunt (R_{sh}) and series (R_s) resistances, ideality factor (*n*) and reverse saturation current density (J_0), with results shown in Figure S16 and Table S1, respectively. R_{sh} and R_s were calculated from the reciprocal of the slopes around the open-circuit and short-circuit regions, respectively. *n* and J_0 were obtained by fitting the dark *J-V* curves with the equation given by:[48]

$$\ln(J_D) = \ln(J_0) + \frac{1}{n}\frac{q}{k_B T}V_b \qquad (1)$$

where J_D is the dark current density, q is the elementary charge, k_B is Boltzmann's constant, T is temperature, and V_b is the applied bias. For the AceMA device, the lower *n* and J_0 indicates a reduced non-radiative trap-mediated recombination and explains the higher V_{OC}, whereas the higher R_{sh} and lower R_s is correlated with the higher FF. We further confirmed the reduced trap density of the AceMA devices using Thermal Admittance Spectroscopy (TAS), where the trap density of states (tDOS) can be calculated from the capacitance-angular frequency relationship using the equation:[49]

$$N_T(E_\omega) = -\frac{V_{bi}}{qW}\frac{dC}{d\omega}\frac{\omega}{kT} \qquad (2)$$

where *C* is the capacitance, ω is the angular frequency, *q* is the elementary charge, *k* is the Boltzmann constant, V_{bi} is the built-in potential, *W* is the depletion width, and *T* is the temperature. As shown in Figure S17, the tDOS for the AceMA device was generally lower than that of the reference MA device, especially in the relatively deeper trap region (0.3 – 0.4 eV), where the minimum tDOS for the AceMA and MA devices reached ~$5\text{x}10^{16}$ m^{-3} eV^{-1} and ~$2\text{x}10^{17}$ m^{-3} eV^{-1}, respectively.

Ion migration and operational stability

In addition to the above discussed observations of reduced ion migration, we set out to directly investigate the ion migration properties of the films through direct current (DC) temperature-dependent conductivity measurements on lateral MA and AceMA devices with structure Au/perovskite (100 µm)/Au to experimentally determine the ion migration activation energies (**Figure 5a** and b). The activation energy (E_a) can be extracted by fitting the raw data points with the Nernst-Einstein equation given by:[17]

$$\sigma(T) = \frac{\sigma_0}{T}\exp(\frac{-E_a}{k_b T}) \qquad (2)$$

where $\sigma(T)$ is the conductivity as a function of temperature T, σ_0 is a constant, and k_b is Boltzmann's constant. Two linear regimes can be seen in the fitted plots of Figure 5a and b. In the low temperature regime, ion migration is essentially suppressed due to the insufficient thermal energy. Above a critical temperature, ion migration became activated and contributed to the exponential enhancement in conductivity. The extracted E_a is 0.542 eV for the AceMA lateral device, a 25% increase over the MA device (0.433 eV). This result complements our DFT calculations discussed before to further support our hypothesis that the lattice distortion caused by substituting MA with Ace resulted in a size-induced steric impediment effect to effectively obstruct the migration of ions in the perovskite.

To assess the operational stability of the AceMA devices, encapsulated solar cell devices were subjected to continuous illumination under 1 sun intensity (no ultraviolet filter) at open-circuit condition in ambient air to test their stability under operational conditions. Ion migration is most severe under open-circuit condition due to the uncompensated built-in potential under illumination.[50,51] In contrast, the applied bias during maximum power point (MPP) tracking is opposite in direction to the built-in voltage and reduces the effective potential gradient.[52] Upon the exclusion of external environmental factors such as moisture and oxygen by proper encapsulation or an inert atmosphere, the instability of PSCs under illumination should be largely due to the migration of mobile ions due to the light-induced potential gradient to degrade the perovskite and adjacent contact layers.[17,19,52–54] For instance, migrating I^- can undergo an irreversible redox reaction to reduce spiro-OMeTAD$^+$ to its neutral state to degrade its p-doping character and thus degrade its hole conductivity and deteriorate the device performance.[53] It was also shown that I^- migrating out of the perovskite layer can deplete I^- from the perovskite layer to rupture its stoichiometry and lattice structure, in addition to reacting with Ag to form AgI to corrode the metal electrode.[54,55]

Figure 5c plots the evolution of the stabilized (steady-state) PCE of the MA and AceMA devices with time. The degradation profiles can be separated into two regimes, where an initial rapid decay is followed by a subsequent near linear decay, similar to what was obscaerved from previous reports.[17,45] From this, the T_{80} (time taken for device steady-state PCE to degrade to 80 % of its initial value) of the devices are obtained by fitting the linear degradation.[17,45] The T_{80} of the AceMA device was calculated to be 2,011 h, a considerable nine-fold improvement over the T_{80} of 222 h of the control MA device. After over 2,100 h of continuous illumination, the AceMA device retained over 55 % of its initial steady-state PCE, compared to only 6.9 % of the MA device after 700 h. The corresponding degradation of the photovoltaic parameters of the devices are also included in Figure S18, which show that the decline in device performance is mainly due to the drop in FF and V_{OC}, whereas the J_{SC} remained relatively constant, consistent with previous reports for devices aged under open-circuit condition.[50,52] Given that degradation of the encapsulated device under illumination at open-circuit condition is largely due to the migration of ionic defects and accumulated charge carriers,[45,52,56] the much improved stability of the AceMA device is probably due to the retarded ion migration as a result of the size-mismatch-induced steric impediment by the large Ace cation.

To assess the thermal stability of the devices, fabricated MA and AceMA devices were subjected to continuous heating at 85 °C in a nitrogen atmosphere and their reverse scan PCEs were measured periodically as shown in Figure 5d. Ag was used as the metal electrode, in which case the migration of I^- towards the electrode to deplete the stoichiometry of the perovskite and the corrosion of the electrode by AgI formation is expected to be the major cause of device degradation,[37,54,55] while the more thermally stable PTAA was used as the hole transporting layer (HTL) to replace spiro-MeOTAD.[8,30,37,57,58] The AceMA device was seen to have significantly improved thermal stability, and retained almost 92 % of its initial PCE after over 450 h of continuous heating. In contrast, the reference MA device degraded to just 1.6 % of its initial PCE over the same time period. Figure S19 includes a breakdown of the evolution of the photovoltaic parameters of the corresponding devices. For the AceMA device, the performance drop is due to the gradually decreasing FF, whereas the V_{OC} and J_{SC} changes negligibly with time. We speculate that the considerable thermal stability enhancement of the AceMA device is likely a result of the impeded migration of I^- due to the size-mismatch-induced lattice distortions. Particularly, we can deduce from the Nernst-Einstein equation above that ion migration is expected to be more severe at higher temperatures due to the supply of thermal energy.

We further exposed the MA and AceMA devices and bare films to controlled environments to investigate their moisture and ambient stabilities. However, we expected their environmental stabilities to be similar due to the comparable hydrogen bonding interaction between MA or Ace with the perovskite lattice. We monitored the X-ray diffractograms and normalized absorbance at 600 nm of the films (Figure S20 and Figure S21) with time exposed to humidity or ambient, which showed that the degradation of AceMA was comparable or slightly enhanced compared to MA. The [(100) perovskite peak]/[PbI_2 peak] intensity ratio of the AceMA film degraded from 14.4 to 0.13 after 59 h exposure to the humid environment, and similarly the MA film degraded from 14.3 to 0.09. For the ambient exposure, the ratio decreased from 14.3 to 4.4 for the MA film and 14.6 to 4.5

for the AceMA film after 136 h exposure. For the devices, the reverse scan PCEs of both the MA and AceMA devices showed no apparent degradation after exposure to humidity or ambient, but the degradation of the devices was obvious through the stabilized PCEs of the devices. Combining the film and device results, we reason that the moisture-induced degradation (defect density generated) was comparable for MA and AceMA, and during the relatively short timescales of the reverse scan, the increased capacitive effects and hysteric behavior of the devices induced by the generated defects were not evident such that the reverse scan PCEs showed no obvious degradation.[17] However, during the longer timescales of the steady-state measurements, defects have sufficient time to migrate in response to the constant bias applied, but for the AceMA devices, due to the steric impediment effect which effectively obstructed defect migration, the capacitive effects was reduced and therefore the degradation of their stabilized PCEs was retarded.

Lastly, the formation enthalpies of the perovskites (supplementary note 2 and Figure S22) were calculated using *ab initio* simulations to assess their intrinsic stability. The more negative formation enthalpy of the $Ace_{0.25}MA_{0.75}PbI_3$ composition demonstrates the improved thermodynamic stability due to the substitution of MA with Ace.

Generalizing the steric impediment of ion migration

To demonstrate the versatility of our proposed steric impediment approach, we generalized the strategy on the commonly used $FAPbI_3$ system. Unlike $MAPbI_3$, the tolerance factor of $FAPbI_3$ is thought to be slightly above the theoretical range to form the cubic phase due to the larger (253 pm) FA cation.[21] Therefore, opposite to the case with $MAPbI_3$, substitution of FA in $FAPbI_3$ for a relatively smaller cation such as MA (217 pm) or Cs (167 pm) can result in improved device operational stability.[22,29,43,59] Using the same procedure, we again measured the temperature-dependent conductivity of fabricated $FAPbI_3$, $MA_{0.05}FA_{0.95}PbI_3$ and $Cs_{0.05}FA_{0.95}PbI_3$ lateral devices to extract the ion migration activation energy. We observed that the activation energy increases in the order

$FAPbI_3$ (0.259 eV) < $MA_{0.25}FA_{0.75}PbI_3$ (0.309 eV) < $Cs_{0.25}FA_{0.75}PbI_3$ (0.467 eV) (Figure S23), correlating with the increasing 'A' cation size mismatch. We additionally modelled the $FAPbI_3$, $MA_{0.25}FA_{0.75}PbI_3$ and $Cs_{0.25}FA_{0.75}PbI_3$ systems using DFT (Figure S24) as before and found that the simulated activation energy followed the trend of $FAPbI_3$ (0.37 eV) < $Cs_{0.25}FA_{0.75}PbI_3$ (0.72 eV) < $MA_{0.25}FA_{0.75}PbI_3$ (0.84 eV). Although both Cs and MA substitution into $FAPbI_3$ increases the energy barrier for iodide migration, the trend does not follow the experimental result. We note that the simulations consider only the iodide migration and do not account for other factors such as perovskite crystallinity, phase purity etc, which is probably the origin of the discrepancy with experimental data. We plan to further investigate this system for a future work.

Conclusions

In this work, we studied the effect of 'A' cation size mismatch induced lattice distortions on the ion migration energetics and operational stability of PSCs by partial substitution of small MA with the larger Ace cation. From our observations, we propose that the size mismatch between Ace and MA introduces localized lattice distortion in the perovskite lattice, which creates a steric effect to effectively impede the migration pathways of ions to increase the migration activation energy barrier. As a result, we observed that the optimized mixed composition $Ace_{0.03}MA_{0.97}PbI_3$ device had much improved thermal stability, retaining 92% of its initial PCE after 450 h under continuous heating at 85 °C, and also significantly elongated operational stability under continuous 1 sun illumination at open-circuit condition in ambient with an extrapolated T_{80} of 2,011 h, relative to the reference pure MA device with a T_{80} of 222 h. We believe our study on this steric engineering strategy would provide essential knowledge to design more operationally stable perovskite compositions.

Experimental Section

Device fabrication

Indium tin oxide (ITO) on glass substrates were cleaned by sonication in detergent, deionized water, acetone, and isopropyl alcohol for 15 min each. For the electron transport layer, the cleaned substrate was treated by ultraviolet ozone for 15 min, and subsequently 30 mM $SnCl_2\cdot 2H_2O$ (98%, Sigma Aldrich) in ethanol (anhydrous, Sigma Aldrich) solution was deposited by spin coating at 3000 rpm for 30 s. The deposited film on substrate was sequentially annealed at 150 ºC for 30 min. Then, a second layer of SnO_2 was deposited, followed by annealing at 150 ºC for 5 min, and lastly 180 ºC for 60 min. For the reference perovskite solution, 1 mmol of CH_3NH_3I (Xi'an Polymer Corp), PbI_2 (TCI, 99.99%), and dimethylsulfoxide (anhydrous, Sigma Aldrich) were dissolved in 500 mg of dimethylformamide (anhydrous, 99.8%, Sigma Aldrich). For the mixed MA/Ace perovskite solution, x mol% (0 < x < 100) of the CH_3NH_3I was substituted with $CH_3C(NH_2)_2^+$ (Sigma Aldrich). To deposit the perovskite thin films, the SnO_2/ ITO substrate was first treated for 15 min by ultraviolet ozone. Spin coating of the perovskite was done in a glovebox filled with dry air. The perovskite solution was spin coated at 4000 rpm for 25 s, and 0.3 mL of diethyl ether (anhydrous, >99.0%, contains BHT as stabilizer, Sigma Aldrich) was dropped after 10 s. The adduct film was annealed at 65 ºC for 1 min, and then 100 ºC for 30 min. For the hole transport layer, spiro-MeOTAD solution was prepared with the following composition: 60.0 mg of spiro-MeOTAD (Xi'an Polymer Corp) was dissolved in 0.7 mL of chlorobenzene (anhydrous, 99.8%, Sigma Aldrich), and added with 25.5 µl of 4-tert-butylpyridine (96%, Sigma Aldrich), 15.5 µl of Li-TFSI salt (99.95%, Sigma Adrich, 520 mg mL^{-1} in acetonitrile) and 12.5 µl of FK209 (Xi'an Polymer Corp, 375 mg mL^{-1} in acetonitrile). Spiro-MeOTAD was also deposited in dry air at 3000 rpm for 30 s. For the top electrode, 80 nm-thick gold was thermally deposited at an evaporation rate of 0.5 A s^{-1}.

Computational study

First-principles calculations of ion migration activation energies were based on the density functional theory (DFT) implemented in the VASP package code.[60,61] A revised Perdew-Burke-Ernzerhof generalized gradient approximation (PBEsol)[62] was used for the exchange-correlation. Dispersion corrections to the total energies are included via Grimme's DFT-D3 scheme.[63,64] Plane-wave expansions with kinetic energies up to 400 eV were selected for all DFT calculation basis sets. Projector-augmented-wave (PAW) pseudopotentials were used to describe valence-core interactions.[65] Both ionic positions and cell dimensions are allowed to relax, using a quasi-Newton algorithm, until the forces are smaller than 0.03 eV/Å. An 8x8x8 r-centered k-point mesh was used for Brillouin-zone sampling.

A supercell with a 2x2x2 periodicity is used in all cases. Iodide migration activation energies are modelled for $CH_3NH_3PbI_3$ and $(CH_3C(NH_2)_2)_{0.25}(CH_3NH_3)_{0.75}PbI_3$, in which for the latter case the $CH_3NH_3I^+$ cation is replaced by a $CH_3C(NH_2)_2^+$ cation in a single cell. A V_I vacancy is initially set in the axial (a) and equatorial (e) positions of a single cage, corresponding to the defect in the initial and final structure, respectively. The migration is activated in the cage centered by $CH_3C(NH_2)_2^+$ in $(CH_3C(NH_2)_2)_{0.25}(CH_3NH_3I)_{0.75}PbI_3$. Initial and final structures are first optimized, then a linear interpolation consisting of 18 grid points between them are employed to define the migration process. The energy profiles are examined using nudged elastic band (NEB) and constrained energy minimization methods. Activation energies are computed from the total energy difference between the initial state and the saddle point.

Material characterization

X-ray diffraction was measured by a X-ray PANalytical diffractometer with Cu Kα radiation at a scan rate of 4 º min-1. The morphology of the perovskite films was characterized by scanning electron microscopy using a Nova Nano 230 instrument. Ultraviolet-visible absorption spectra were recorded by U-4100 spectrophotometer (Hitachi) equipped with integrating sphere. The photoluminescence (PL) spectra was analyzed by a Horiba Jobin Yvon system, where a 640 nm monochromatic laser was used as an excitation source. Time resolved photoluminescence spectra were obtained using a Picoharp 300 with time-correlated single-photon counting capabilities. Perovskite films on glass were excited by a 640 nm pulse laser with a repetition frequency of 200 kHz provided by a picosecond laser diode head (PLD 800B, PicoQuant). The temperature-dependent conductivity measurement was performed using a commercial probe station (Lakeshore, TTP4) where the device temperature was controlled with a thermoelectric plate and flow of liquid nitrogen. The electrical measurement was done with a Agilent, B2902A source/measurement unit.Data availability. The authors declare that the data supporting the findings of this study are available within the paper and its supplementary information files.

Device characterization

A Keithley 2401 source meter was used to measure the current density–voltage (*J*–*V*) responses of the devices under simulated one sun AM 1.5G illumination (100 mW cm^{-2}) from an Oriel Sol3A class AAA solar simulator (Newport). The devices were measured in ambient air. The light intensity was calibrated with a NREL-certified Si photodiode with a KG-5 filter. A 0.100 cm^{2} sized metal aperture was used to precisely define the device active area during measurement at a scan rate of 0.1 V s^{-1} from 1.2 V to -0.1 V. All devices were measured without any preconditioning including light soaking and applied bias voltage. Steady-state power output was calculated by measuring the stabilized photocurrent density at a constant applied bias. The external quantum efficiency (EQE) was measured with a specially designed system (Enlitech) under alternating current mode (frequency = 133 Hz) without light bias. The transient photovoltage was measured with a pulsed red dye laser (Rhodamine 6G, 590nm) pumped by a nitrogen laser (LSI VSL-337ND-S) as the perturbation source. The pulse width was 4 ns at a repetition frequency of 10 Hz. The laser pulse intensity was monitored to maintain the amplitude of transient V_{OC} below 5 mV. Then, the open circuit voltage was measured with a 1 MΩ resistor, and recorded on a digital oscilloscope (Tektronix DPO 4104B).

Supporting Information

Supporting Information is available from the Wiley Online Library or from the author.

Acknowledgements

This work was supported by the U.S. Department of Energy's Office of Energy Efficiency and Renewable Energy (EERE) under the Solar Energy Technologies Office under award number DE-EE0008751. Computing resources used in this work were provided by the National Center for High Performance Computing of Turkey (UHEM) with grant number 5005902018.

Received: ((will be filled in by the editorial staff))
Revised: ((will be filled in by the editorial staff))
Published online: ((will be filled in by the editorial staff))

References

[1] A. Kojima, K. Teshima, Y. Shirai, T. Miyasaka, *J. Am. Chem. Soc.* **2009**, *131*, 6050.

[2] H.-S. Kim, C.-R. Lee, J.-H. Im, K.-B. Lee, T. Moehl, A. Marchioro, S.-J. Moon, R. Humphry-Baker, J.-H. Yum, J. E. Moser, M. Grätzel, N.-G. Park, *Sci. Rep.* **2012**, *2*, 1.

[3] M. M. Lee, J. Teuscher, T. Miyasaka, T. N. Murakami, H. J. Snaith, *Science* **2012**, *338*, 643.

[4] J. Burschka, N. Pellet, S.-J. Moon, R. Humphry-Baker, P. Gao, M. K. Nazeeruddin, M. Grätzel, *Nature* **2013**, *499*, 316.

[5] W. S. Yang, B.-W. Park, E. H. Jung, N. J. Jeon, Y. C. Kim, D. U. Lee, S. S. Shin, J. Seo, E. K. Kim, J. H. Noh, S. Il Seok, *Science* **2017**, *356*, 1376.

[6] H. Tan, A. Jain, O. Voznyy, X. Lan, F. P. G. de Arquer, J. Z. Fan, R. Quintero-Bermudez, M. Yuan, B. Zhang, Y. Zhao, F. Fan, P. Li, L. N. Quan, Y. Zhao, Z.-H. Lu, Z. Yang, S. Hoogland, E. H. Sargent, *Science* **2017**, *355*, 722.

[7] M. Kim, G. Kim, K. T. Lee, I. W. Choi, H. W. Choi, Y. Jo, Y. J. Yoon, J. W. Kim, J. Lee, D. Huh, H. Lee, S. K. Kwak, J. Y. Kim, D. S. Kim, *Joule* **2019**, *3*, 1.

[8] Q. Jiang, Y. Zhao, X. Zhang, X. Yang, Y. Chen, Z. Chu, Q. Ye, X. Li, Z. Yin, J. You, *Nat. Photonics* **2019**, *13*, 460.

[9] Z. Song, A. Abate, S. C. Watthage, G. K. Liyanage, A. B. Phillips, U. Steiner, M. Grätzel, M. J. Heben, *Adv. Energy Mater.* **2016**, *6*, 1.

[10] J. Yang, B. D. Siempelkamp, D. Liu, T. L. Kelly, *ACS Nano* **2015**, *9*, 1955.

[11] J. A. Christians, P. A. M. Herrera, P. V Kamat, *J. Am. Chem. Soc.* **2015**, *137*, 1530.

[12] D. Bryant, N. Aristidou, S. Pont, I. Sanchez-molina, T. Chotchunangatchaval, S. Wheeler, R.

Durrant, S. A. Haque, *Energy Environ. Sci.* **2016**, *9*, 1655.

[13] B. Conings, J. Drijkoningen, N. Gauquelin, A. Babayigit, J. D'Haen, L. D'Olieslaeger, A. Ethirajan, J. Verbeeck, J. Manca, E. Mosconi, F. De Angelis, H.-G. Boyen, *Adv. Energy Mater.* **2015**, *5*, 1.

[14] W.-J. Yin, T. Shi, Y. Yan, *Appl. Phys. Lett.* **2014**, *104*, 1.

[15] J. M. Azpiroz, E. Mosconi, J. Bisquert, F. De Angelis, *Energy Environ. Sci.* **2015**, *8*, 2118.

[16] C. Eames, J. M. Frost, P. R. F. Barnes, B. C. O'Regan, A. Walsh, M. S. Islam, *Nat. Commun.* **2015**, *6*, 1.

[17] K. Domanski, B. Roose, T. Matsui, M. Saliba, S. H. Turren-Cruz, J. P. Correa-Baena, C. R. Carmona, G. Richardson, J. M. Foster, F. De Angelis, J. M. Ball, A. Petrozza, N. Mine, M. K. Nazeeruddin, W. Tress, M. Grätzel, U. Steiner, A. Hagfeldt, A. Abate, *Energy Environ. Sci.* **2017**, *10*, 604.

[18] K. Domanski, J.-P. Correa-Baena, N. Mine, M. K. Nazeeruddin, A. Abate, M. Saliba, W. Tress, A. Hagfeldt, M. Grätzel, *ACS Nano* **2016**, *10*, 6306.

[19] J.-W. Lee, S.-G. Kim, J.-M. Yang, Y. Yang, N.-G. Park, *APL Mater.* **2019**, *7*, 1.

[20] G. E. Eperon, S. D. Stranks, C. Menelaou, M. B. Johnston, L. M. Herz, H. J. Snaith, *Energy Environ. Sci.* **2014**, *7*, 982.

[21] J.-W. Lee, D.-J. Seol, A.-N. Cho, N.-G. Park, *Adv. Mater.* **2014**, *26*, 4991.

[22] J.-W. Lee, D.-H. Kim, H.-S. Kim, S.-W. Seo, S. M. Cho, N.-G. Park, *Adv. Energy Mater.* **2015**, *5*, 1.

[23] C. Lin, S. Li, W. Zhang, C. Shao, Z. Yang, *ACS Appl. Energy Mater.* **2018**, *1*, 1374.

[24] R. Ruess, F. Benfer, F. Bçcher, M. Stumpp, D. Schlettwein, *ChemPhysChem* **2016**, *17*, 1505.

[25] J. H. Noh, S. H. Im, J. H. Heo, T. N. Mandal, S. Il Seok, *Nano Lett.* **2013**, *13*, 1764.

[26] S. Pont, D. Bryant, C.-T. Lin, N. Aristidou, S. Wheeler, X. Ma, R. Godin, S. A. Haque, J. R. Durrant, *J. Mater. Chem. A* **2017**, *5*, 9553.

[27] M. C. Brennan, S. Draguta, P. V Kamat, M. Kuno, *ACS Energy Lett.* **2018**, *3*, 204.

[28] A. D. Jodlowski, C. Roldán-carmona, G. Grancini, M. Salado, M. Ralaiarisoa, S. Ahmad, N. Koch, L. Camacho, G. De Miguel, M. K. Nazeeruddin, *Nat. Energy* **2017**, *2*, 972.

[29] M. Saliba, T. Matsui, J.-Y. Seo, K. Domanski, J.-P. Correa-Baena, M. K. Nazeeruddin, S. M. Zakeeruddin, W. Tress, A. Abate, A. Hagfeldt, M. Grätzel, *Energy Environ. Sci.* **2016**, *9*, 1989.

[30] M. Saliba, T. Matsui, K. Domanski, J.-Y. Seo, A. Ummadisingu, S. M. Zakeeruddin, J. P. Correa-Baena, W. Tress, A. Abate, A. Hagfeldt, M. Grätzel, *Science* **2016**, *354*, 206.

[31] D. W. Ferdani, S. R. Pering, D. Ghosh, P. Kubiak, A. B. Walker, S. E. Lewis, A. L. Johnson, P. J. Baker, M. S. Islam, P. J. Cameron, *Energy Environ. Sci.* **2019**, *12*, 2264.

[32] C. C. Stoumpos, L. Frazer, D. J. Clark, Y. S. Kim, S. H. Rhim, A. J. Freeman, J. B. Ketterson, J. I. Jang, M. G. Kanatzidis, *J. Am. Chem. Soc.* **2015**, *137*, 6804.

[33] G. Kieslich, S. Sun, A. K. Cheetham, *Chem. Sci.* **2014**, *5*, 4712.

[34] P. S. Whitfield, N. Herron, W. E. Guise, K. Page, Y. Q. Cheng, I. Milas, M. K. Crawford, *Sci. Rep.* **2016**, *6*, 1.

[35] A. Amat, E. Mosconi, E. Ronca, C. Quarti, P. Umari, K. Nazeeruddin, M. Gra, F. De Angelis, *Nano Lett.* **2014**, *14*, 3608.

[36] E. Arunan, G. R. Desiraju, R. A. Klein, J. Sadlej, S. Scheiner, I. Alkorta, D. C. Clary, R. H. Crabtree, J. J. Dannenberg, P. Hobza, H. G. Kjaergaard, A. C. Legon, B. Mennucci, D. J. Nesbitt,

Pure Appl. Chem. **2011**, *83*, 1637.

[37] R. Wang, J. X. Xue, L. Meng, J.-W. Lee, Z. Zhao, P. Sun, L. C. Cai, T. Huang, Z. Wang, Z.-K. W. Wang, Y. D. Duan, J. L. Yang, S. Tan, Y. Yuan, Y. Huang, Y. Yang, *Joule* **2019**, *3*, 1464.

[38] J. Haruyama, K. Sodeyama, L. Han, Y. Tateyama, *J. Am. Chem. Soc.* **2015**, *137*, 10048.

[39] N. Pellet, P. Gao, G. Gregori, T. Yang, M. K. Nazeeruddin, J. Maier, M. Grätzel, *Angew. Chemie Int. Ed.* **2014**, *53*, 3151.

[40] Z. Li, M. Yang, J.-S. Park, S.-H. Wei, J. J. Berry, K. Zhu, *Chem. Mater.* **2016**, *28*, 284.

[41] J.-W. Lee, D.-K. Lee, D.-N. Jeong, N.-G. Park, *Adv. Funct. Mater.* **2018**, *1807047*, 1.

[42] H. W. Qiao, S. Yang, Y. Wang, X. Chen, T. Y. Wen, L. J. Tang, Q. Cheng, Y. Hou, H. Zhao, H. G. Yang, *Adv. Mater.* **2019**, *31*, 1.

[43] X. Zheng, C. Wu, S. K. Jha, Z. Li, K. Zhu, S. Priya, *ACS Energy Lett.* **2016**, *1*, 1014.

[44] H. Chen, Q. Wei, M. I. Saidaminov, F. Wang, A. Johnston, Y. Hou, Z. Peng, K. Xu, W. Zhou, Z. Liu, L. Qiao, X. Wang, S. Xu, J. Li, R. Long, Y. Ke, E. H. Sargent, Z. Ning, *Adv. Mater.* **2019**, *31*, 1.

[45] J.-W. Lee, Z. Dai, T.-H. Han, C. Choi, S. Y. Chang, S. J. Lee, N. De Marco, H. Zhao, P. Sun, Y. Huang, Y. Yang, *Nat. Commun.* **2018**, *9*, 1.

[46] D. Shi, V. Adinolfi, R. Comin, M. Yuan, E. Alarousu, A. Buin, Y. Chen, S. Hoogland, A. Rothenberger, K. Katsiev, Y. Losovyj, X. Zhang, P. A. Dowben, O. F. Mohammed, E. H. Sargent, O. M. Bakr, *Science* **2015**, *347*, 519.

[47] D.-Y. Son, J.-W. Lee, Y. J. Choi, I.-H. Jang, S. Lee, P. J. Yoo, H. Shin, N. Ahn, M. Choi, D. Kim, N.-G. Park, *Nat. Energy* **2016**, *1*, 1.

[48] H.-W. Kang, J.-W. Lee, D.-Y. Son, N.-G. Park, *RSC Adv.* **2015**, *5*, 47334.

[49] J. Lee, S. Bae, Y. Hsieh, N. De, M. Wang, J. Lee, S. Bae, Y. Hsieh, N. De Marco, M. Wang, *Chem* **2017**, *3*, 290.

[50] K. Domanski, E. A. Alharbi, A. Hagfeldt, M. Grätzel, W. Tress, *Nat. Energy* **2018**, *3*, 61.

[51] W. Nie, J. Blancon, A. J. Neukirch, K. Appavoo, H. Tsai, M. Chhowalla, M. A. Alam, M. Y. Sfeir, C. Katan, J. Even, S. Tretiak, J. J. Crochet, G. Gupta, A. D. Mohite, *Nat. Commun.* **2016**, *7*, 1.

[52] M. V. Khenkin, A. K.M., E. A. Katz, I. Visoly-Fisher, *Energy Environ. Sci.* **2019**, *12*, 550.

[53] J. Carrillo, A. Guerrero, S. Rahimnejad, O. Almora, I. Zarazua, E. Mas-marza, J. Bisquert, G. Garcia-belmonte, *Adv. Energy Mater.* **2016**, *6*, 1.

[54] A. F. Akbulatov, L. A. Frolova, M. P. Griffin, I. R. Gearba, A. Dolocan, D. A. Vanden Bout, S. Tsarev, E. A. Katz, A. F. Shestakov, K. J. Stevenson, P. A. Troshin, *Adv. Energy Mater.* **2017**, *7*, 1.

[55] C. Besleaga, L. E. Abramiuc, V. Stancu, A. G. Tomulescu, M. Sima, L. Trinca, N. Plugaru, L. Pintilie, G. A. Nemnes, M. Iliescu, H. Gud, A. Manolescu, I. Pintilie, *J. Phys. Chem. Lett.* **2016**, *7*, 5168.

[56] N. Ahn, K. Kwak, M. S. Jang, H. Yoon, B. Y. Lee, J. K. Lee, P. V Pikhitsa, J. Byun, M. Choi, *Nat. Commun.* **2016**, *7*, 1.

[57] J. Xue, R. Wang, K. Wang, Z. Wang, I. Yavuz, Y. Wang, Y. Yang, X. Gao, T. Huang, S. Nuryyeva, J. Lee, Y. Duan, L. Liao, R. Kaner, Y. Yang, *J. Am. Chem. Soc.* **2019**, *141*, 13948.

[58] T. Han, S. Tan, J. Xue, L. Meng, J. Lee, Y. Yang, *Adv. Mater.* **2019**, *31*, 1.

[59] C. Yi, J. Luo, S. Meloni, A. Boziki, N. Ashari-Astani, C. Gratzel, S. M. Zakeeruddin, U. Rothlisberger, M. Grätzel, *Energy Environ. Sci.* **2016**, *9*, 656.

[60] G. Kresse, J. Furthmuller, *Comput. Mater. Sci.* **1996**, *6*, 15.

[61] G. Kresse, J. Furthmuller, *Phys. Rev. B* **1996**, *54*, 11169.

[62] J. P. Perdew, K. Burke, M. Ernzerhof, *Phys. Rev. Lett.* **1996**, *77*, 3865.

[63] S. Grimme, *J. Comput. Chem.* **2006**, *27*, 1787.

[64] S. Grimme, J. Antony, S. Ehrlich, H. Krieg, *J. Chem. Phys.* **2010**, *132*, 1.

[65] P. E. Blöchl, *Phys. Rev. B* **1994**, *50*, 17953.

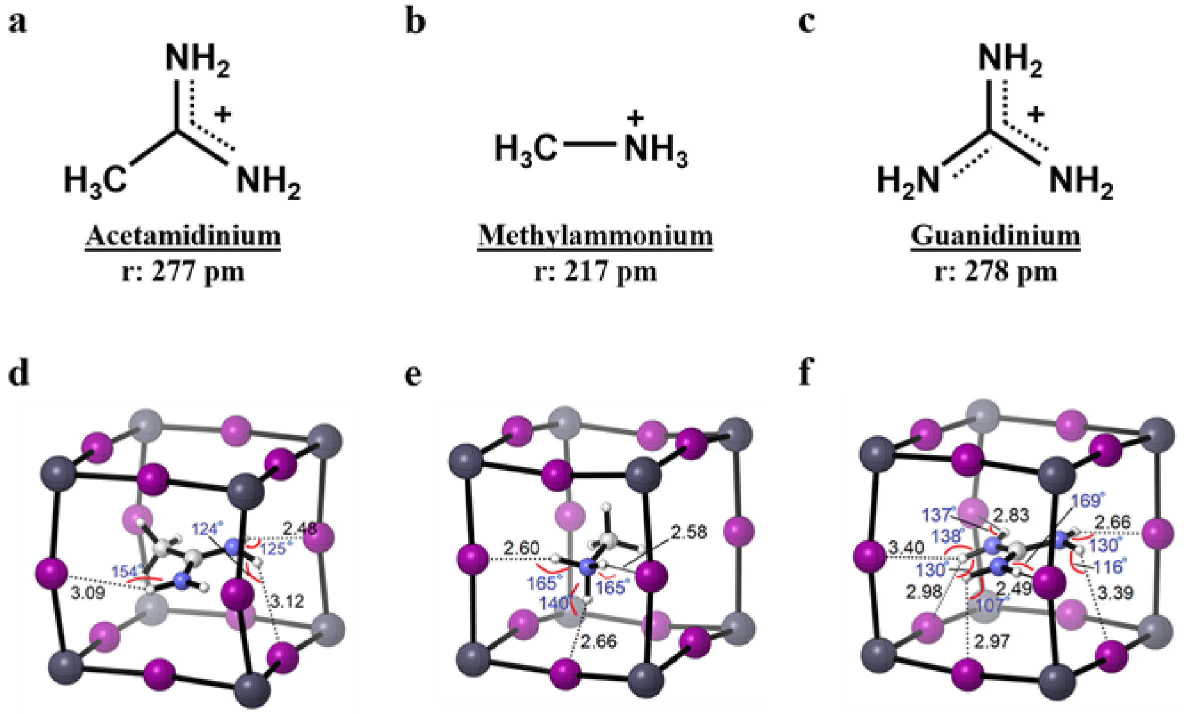

Figure 1. Chemical structures of a) acetamidinium, b) methylammonium, and c) guanidinium. Density functional theory (DFT) modelled effective hydrogen bonds between the 'A' cations and perovskite lattice for d) acetamidinium, e) methylammonium, and f) guanidinium. Black numbers are the bond lengths (in angstroms) and blue numbers are the bond angles (in degrees).

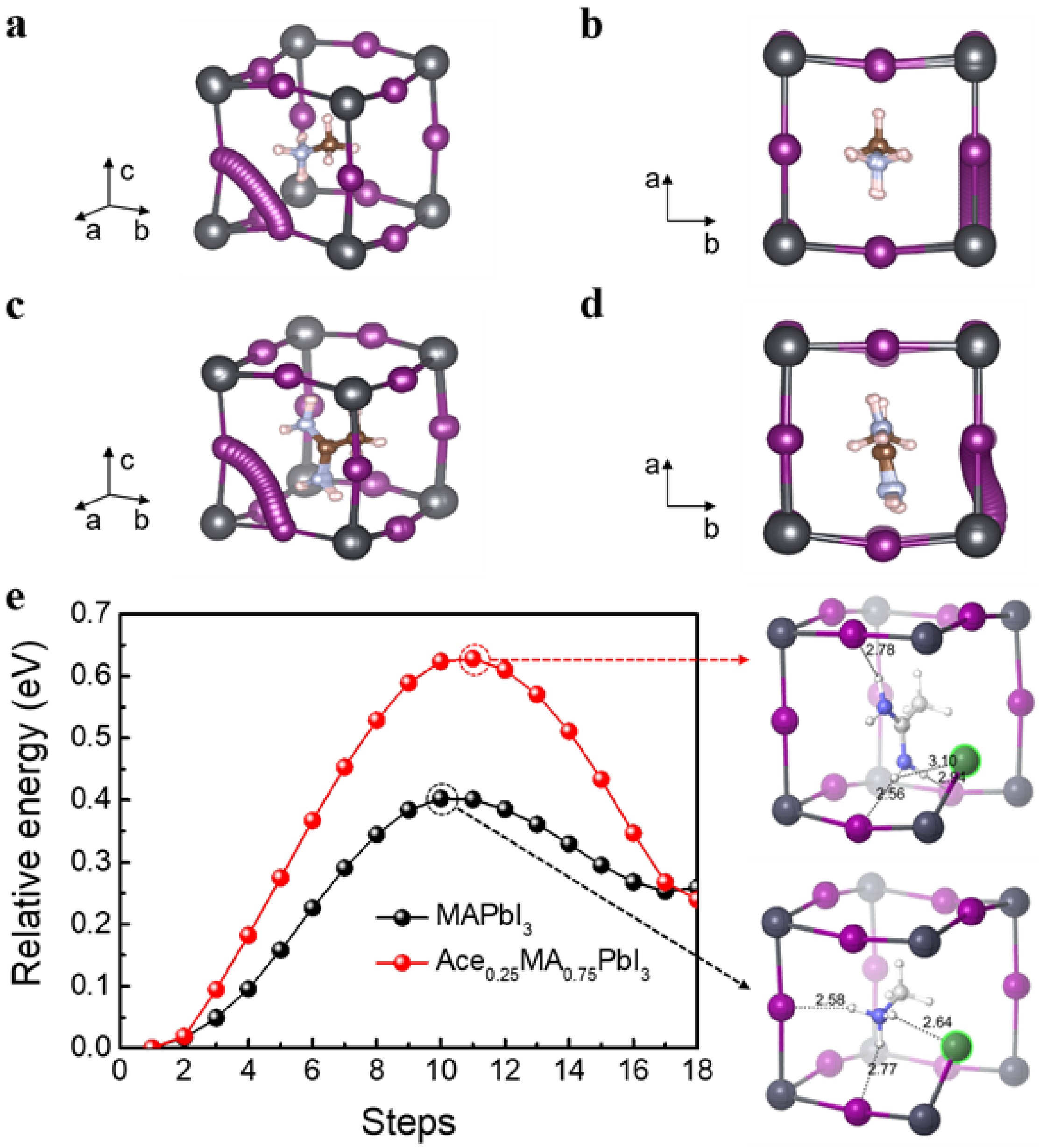

Figure 2. Density functional theory (DFT) modelled a) side view and b) top view iodide ion migration pathway for $MAPbI_3$ perovskite and c) side view and d) top view iodide ion migration pathway for $Ace_{0.25}MA_{0.75}PbI_3$ perovskite, showing only the unit cell containing the Ace cation. e) Iodide ion migration activation energy for $MAPbI_3$ and $Ace_{0.25}MA_{0.75}PbI_3$ calculated using DFT. Included are the transition states corresponding to the maximum energy states, showing the hydrogen bond length between the migrating iodide ion (highlighted in green) and the nearest neighbouring hydrogen atom.

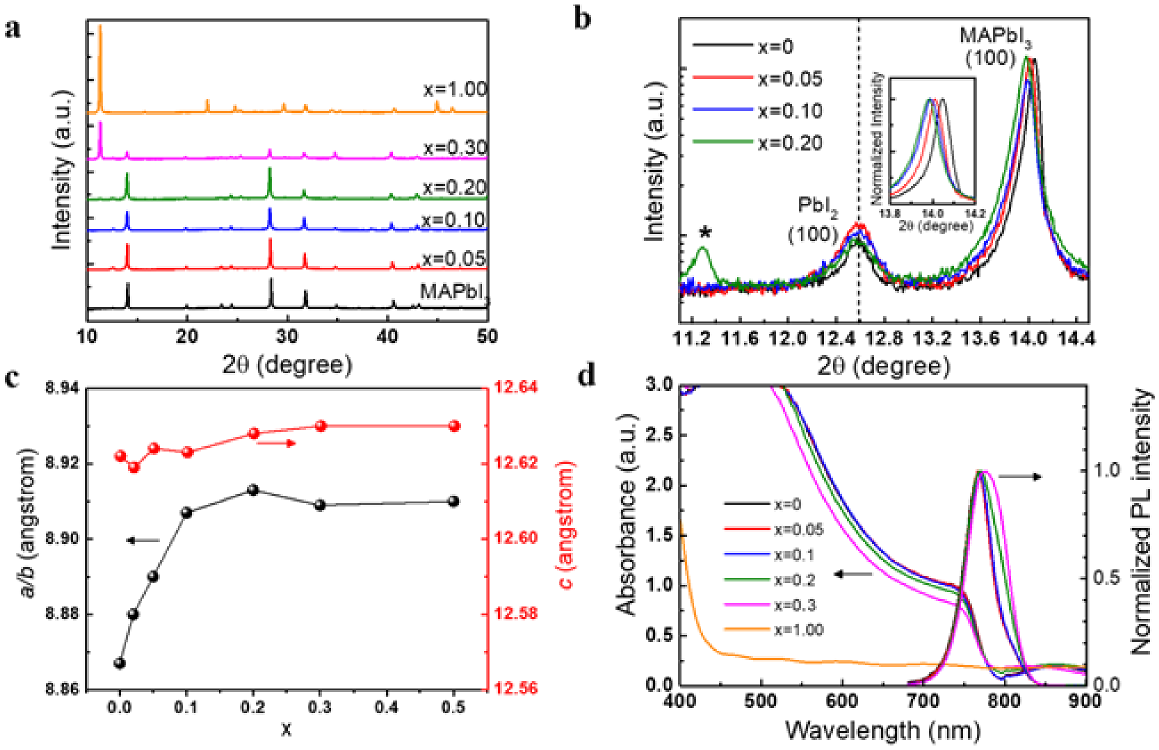

Figure 3. a) X-ray diffraction (XRD) spectra of the $Ace_xMA_{1-x}PbI_3$ films with different values of x. b) High-resolution XRD spectra of the perovskite films showing the (100) perovskite diffraction peak. The PbI_2 and secondary phase (*) diffraction peaks are labelled. Inset shows the magnified normalized (100) perovskite peak. c) Variation of the *a* (or b) and *c* unit cell lattice parameters of the $Ace_xMA_{1-x}PbI_3$ films with different values of x. d) Absorption and normalized photoluminescence spectra of the $Ace_xMA_{1-x}PbI_3$ films with different values of x.

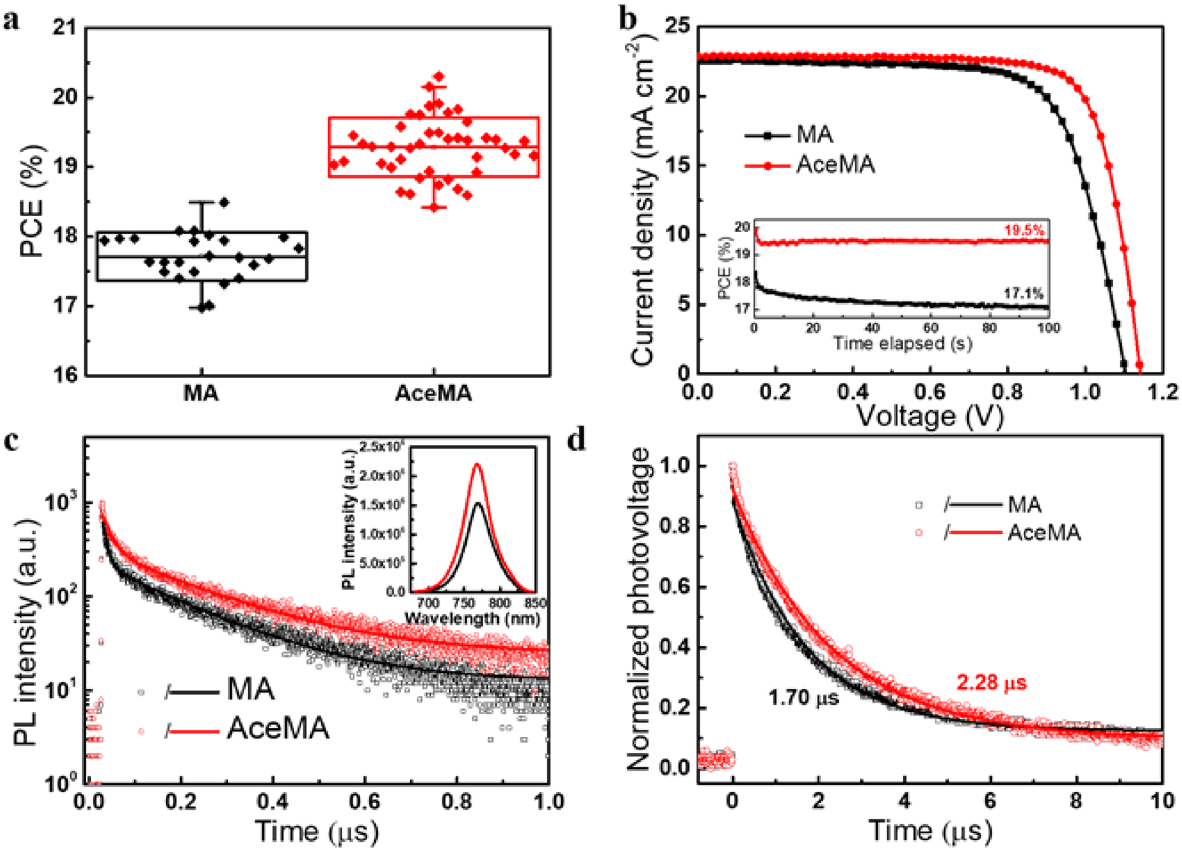

Figure 4. a) Box plot showing the power conversion efficiency (PCE) distribution of the $MAPbI_3$ and $Ace_{0.03}MA_{0.97}PbI_3$ devices. b) Current density and voltage (*J-V*) curves of the champion devices. Inset includes the stabilized PCEs. c) Time-resolved photoluminescence spectra of the MA and AceMA films. Solid lines are the fitted profiles using a bi-exponential decay function. Inset includes the steady-state PL spectra. d) Transient photovoltage decay of the MA and AceMA devices. Solid lines are the fitted profiles using a mono-exponential decay function.

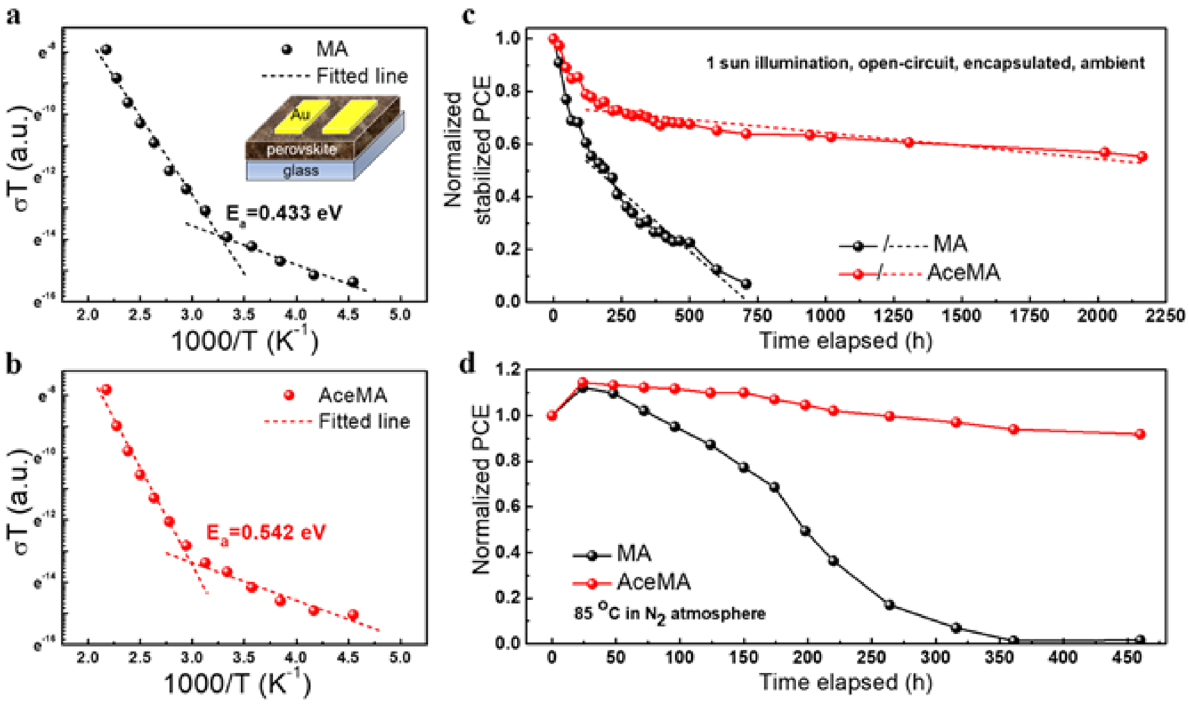

Figure 5. Temperature-dependant conductivity of the a) $MAPbI_3$ and b) $Ace_{0.03}MA_{0.97}PbI_3$ lateral devices. c) Operational stability testing of encapsulated $MAPbI_3$ and $Ace_{0.03}MA_{0.97}PbI_3$ devices under continuous 1 sun illumination under open-circuit condition in ambient air. d) Thermal stability testing of the $MAPbI_3$ and $Ace_{0.03}MA_{0.97}PbI_3$ devices heated continuously at 85 °C in a nitrogen atmosphere.

Table 1. Density functional theory simulated effective bond lengths and bond angles of the 'A' cations with the perovskite lattice. Included are the average bond lengths and bond angles.

	Acetamidinium (Ace)		**Methylammonium (MA)**		**Guanidinium (GA)**	
Number	**Bond length (Å)**	**Bond angles (°)**	**Bond length (Å)**	**Bond angles (°)**	**Bond length (Å)**	**Bond angles (°)**
1	3.10	154	2.60	165	3.00	150
2	3.12	124	2.60	165	2.49	170
3	2.50	126	2.7	140	3.40	116
4					2.70	130
5					2.83	136
6					2.98	130
7					3.40	137
Average	2.91	135	2.63	157	2.97	138

Table 2. Average photovoltaic parameters of the $Ace_xMA_{1-x}PbI_3$ devices, summarizing the short-circuit current density (J_{SC}), open-circuit voltage (V_{OC}), fill factor (FF), power conversion efficiency (PCE), and best PCE.

	J_{SC} (mA cm^{-2})	V_{OC} (V)	FF	PCE (%)	Best PCE (%)
0	22.59 ± 0.14	1.105 ± 0.007	0.710 ± 0.012	17.72 ± 0.34	18.49
2	22.58 ± 0.13	1.134 ± 0.007	0.743 ± 0.006	19.03 ± 0.27	19.65
3	22.67 ± 0.15	1.134 ± 0.009	0.750 ± 0.013	19.28 ± 0.44	20.30
5	22.49 ± 0.15	1.143 ± 0.015	0.728 ± 0.015	18.60 ± 0.62	19.36
8	22.68 ± 0.25	1.136 ± 0.008	0.732 ± 0.008	18.86 ± 0.26	19.23
10	22.22 ± 0.46	1.132 ± 0.015	0.721 ± 0.004	18.16 ± 0.58	18.83
15	21.92 ± 0.23	1.124 ± 0.010	0.712 ± 0.007	17.53 ± 0.41	18.04
20	22.01 ± 0.25	1.128 ± 0.019	0.710 ± 0.014	17.63 ± 0.32	18.17

Table 3. Time-resolved photoluminescence decay parameters for the $MAPbI_3$ and $Ace_{0.03}MA_{0.97}PbI_3$ films on glass fitted using a bi-exponential decay model.

	A_1	Proportion (%)	τ_1 (ns)	A_2	Proportion (%)	τ_2 (ns)	τ_{ave} (ns)
MA	1065.0	83.6	10.4	208.5	16.4	180.7	38.3
AceMA	951.9	76.0	20.4	300.2	24.0	205.9	64.9

A steric engineering strategy to impede ion migration in perovskite thin films is demonstrated where ion migration was effectively hindered by localized lattice distortions induced by incorporation of oversized A site cations. The steric engineering approach improved the operational lifetime of perovskite solar cells by more than nine-fold from 222 h to 2,011h.

Perovskite solar cells

Shaun Tan, Ilhan Yavuz, Nicholas De Marco, Tianyi Huang, Sung-Joon Lee, Christopher S. Choi, Minhuan Wang, Selbi Nuryyeva, Rui Wang, Yepin Zhao, Hao-Cheng Wang, Tae-Hee Han, Bruce Dunn, Yu Huang, Jin-Wook Lee and Yang Yang**

Steric Impediment of Ion Migration Contributes to Improved Operational Stability of Perovskite Solar Cells

55 mm broad × 50 mm high